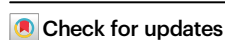






History of individual presolar SiC grains revealed by stellar winds

Received: 15 November 2024

Accepted: 10 September 2025

Published online: 14 October 2025

Ken-ichi Bajo ¹, Tatsuki Izumi¹, Yuta Otsuki ¹, Sachiko Amari ² & Hisayoshi Yurimoto ^{1,3} 

Asymptotic giant branch (AGB) stars, which are evolved low- to intermediate-mass stars, rank among the most prolific producers of interstellar dust in the Galaxy. Presolar silicon carbide (SiC) grains in meteorites are mainly produced by AGB stars. These presolar grains contain abundant noble gases, believed to have been implanted by stellar winds from the central stars of planetary nebulae (CSPNe). Here we report 3-D maps of the helium distribution in individual presolar SiC grains. The maps reveal that the implantation energy of ⁴He for individual grains varies from about 2 to about 4 keV/nucleon, which falls within the range of the CSPN winds. The variation of ⁴He fluence (1×10^{12} – 2×10^{15} atom cm⁻²) shows that the SiC grains form during the last about 1 My period of the AGB star phase. Then, they migrate outwards and become exposed to CSPN winds at distances of 0.3–32 light-years from the CSPNe.

Presolar grains, found in primitive chondrites, had apparently formed around late-type stars before the Solar System formation¹. They were present in the parent molecular cloud of our Solar System after interstellar travel from their stellar site of origin. Analysis of presolar grains would provide clues about how dusts form and survive in the Galaxy¹. Silicon carbide (SiC) is one of the major phases among presolar grains found in primitive chondrites^{2,3}. Based on their isotopic abundances of elements measured in the grains, most of presolar SiC (about 93% of the total number, mainstream SiC) is thought to have originated from low-mass (about 1–3 Solar mass, M_{\odot}) late-type stars in the asymptotic giant branch (AGB) phase of evolution^{4–9}, which eject large amounts of gas into space and are one of the major contributors to the interstellar dusts¹⁰. The formation and growth of the mainstream SiC occurred at 2–6 stellar radii in the circumstellar envelopes of AGB stars¹¹. The formed SiC grains migrate outwards into interstellar space with the expanding envelopes. The residence time spent in the interstellar space for each grain was estimated from the interstellar cosmic ray exposure age, which ranged from 3.9 My to 3 Gy, with a median of 0.2 Gy^{12–14}.

The mainstream SiC grains contain noble gases of a close-to-solar component corresponding to the composition of AGB star envelope (Ne-N and He-N), and an anomalous component corresponding to the

composition of AGB-star He-shells (Ne-G and He-G)^{6,15}. The G-components account for more than 95% of the total. The noble gases appear to have been physically implanted after grain formation. The implantation would be caused by irradiations of stellar winds during the evolutionary stage of low-mass stars, from the AGB phase to the central stars of planetary nebulae (CSPNe) phase. The origins of the stellar winds can be inferred from the implantation energies of noble gases, which are directly calculated from the kinetic energy associated with the stellar wind velocities.

Verchovsky et al.¹⁶ investigated the implanted energy based on the grain size dependence of the noble gas bulk concentrations between size-sorted SiC grains from the Murchison meteorite, assuming a near constant implantation energy. The implantation energy of He- and Ne-N was calculated to be about 10 keV/nucleon (corresponding to a stellar wind speed of about 1400 km s⁻¹), while that of He- and Ne-G was about 50 keV/nucleon (corresponding to a stellar wind speed of about 3000 km s⁻¹)¹⁶. Verchovsky et al.¹⁶ suggest that the lower implantation energy corresponds to the stellar winds of carbon stars, and the higher energy corresponds to the stellar winds of CSPNe, according to the stellar evolution of AGB stars¹⁷ and the formation of mainstream SiC¹¹. On the other hand, the stellar winds could be highly variable from about 5 to about 40 km s⁻¹ for AGB stars^{18–21} and

¹Department of Earth and Planetary Sciences, Faculty of Science, Hokkaido University, Sapporo, Japan. ²Department of Physics & McDonnell Center for the Space Sciences, Campus Box 1105, Washington University, One Brookings Drive, St. Louis, MO, USA. ³Natural History Sciences & Isotope Imaging Laboratory (IIL), Hokkaido University, Sapporo, Japan. ✉e-mail: yuri@ep.sci.hokudai.ac.jp

Table 1 | Carbon isotope ratios and total ^4He counts of SiC grain from Murchison

Grain	size / μm	$^{12}\text{C}/^{13}\text{C}$	σ	Acc pixels	^4He	b.g.	SE	^4He -b.g.	S/N	Remarks
A3-01a	2.7	37.4	11.7	6	503	11	3	492	164	
A3-01b	1.8	41.2	12.2	6	305	11	3	294	98	
A3-02	2.2	32.4	3.5	49	101	47	7	54	8	
A3-03	2.2	28.0	3.5	49	104	47	7	57	8	
A3-04	1.1	42.2	5.8	15	121	85	11	36	3	b.d.
A3-05	0.9	49.4	6.5	20	170	113	12	57	5	
A3-06	1.1	87.2	14.1	20	183	113	12	70	6	
A3-07	0.6	47.6	9.2	20	214	113	12	101	8	
A3-09a	2.0	58.7	5.9	48	101	68	10	33	3	b.d.
A3-09b	2.8	41.6	8.4	16	19	16	3	3	1	b.d.
A3-10	1.6	28.7	2.8	80	369	250	16	119	7	
A3-11	1.5	62.9	3.7	42	203	98	12	105	9	
A3-12a	3.6	12.6	3.8	42	5876	361	30	5515	184	
A3-12b	1.8	16.3	6.7	20	794	177	21	617	29	*
A3-12c	1.8	20.8	7.4	42	596	361	30	235	8	
average	1.8	40.5	19.4							
median	1.8	41.2								
max	3.6	87.2								
min	0.6	12.6								

Acc pixels Accumulated pixels for depth profiling, b.g. background, SE standard error of b.g., b.d. below detection limit. * ^4He signals were obscured by intense ^4He signals from adjacent SiC grains.

from about 20 to about 3000 km s^{-1} for CSPNe^{22–26}. In order to study the variations in implantation energy into each presolar grain caused by stellar winds, it is essential to measure the implantation profiles of individual mainstream SiC grains. However, previous studies for individual grains^{15,27–29} have only measured by melting a whole SiC grain all at once. By that method, depth profiles of noble gases could not be obtained.

Here, we show three-dimensional (3-D) maps of ^4He distribution in individual mainstream SiC grains. From the maps, we analyze the implanted distribution of ^4He into the grains and determine the implantation energies and the fluences for each grain. The results reveal the history of individual presolar SiC grains, suggesting that the grains form near their parent AGB-stars during the last about 1 My period of the AGB star phase. The grains are then carried outward with the expanding circumstellar envelopes of the AGB stars. After traveling 0.3 to 32 light-years, the CSPN winds become implanted into the grains.

Results and discussion

Three-dimensional analysis of presolar SiC grains

We have developed a new secondary neutral mass spectrometer (SNMS) for analyzing He with nanometer-scale resolution, called LIMAS³⁰. LIMAS revealed the depth profile of the solar wind He implanted in the NASA Genesis target and derived the fluence spectra of the solar wind³¹. Here we analyzed 15 presolar SiC grains, which were aliquoted from a size-sorted fraction called KJG extracted from the Murchison carbonaceous meteorite³². The aliquot was dispersed on a gold plate using a droplet of a mix of distilled water and isopropyl alcohol (see methods, subsection ‘Sample and sample preparation’ for details). We determined, for the first time, the 3-D distribution of ^4He together with ^{12}C , ^{13}C , and ^{28}Si , ^{29}Si , ^{30}Si of the individual presolar SiC grains using LIMAS to derive their depth profiles to deduce when, where, and how He was incorporated into presolar SiC grains (see methods, subsection ‘3-D helium analysis by LIMAS’ for details).

Determining stellar wind speeds from 3-D analysis

The measured $^{12}\text{C}/^{13}\text{C}$ ratios of presolar SiC grains are unimodally distributed over the range from 12 to 87 with an average of 41 (Table 1).

This distribution is similar to those of mainstream SiC⁵, indicating that these grains likely belong to mainstream SiC. This is reasonable because about 93% of presolar SiC is accounted for by mainstream SiC⁵. The 3 SiC grains (A3-04, A3-09a, and A3-09b) were undetected ^4He from the grains, and the ^4He signals from the grain (A3-12b) were interfered with by the intense ^4He signals from an adjacent SiC grain, but the other 11 grains contain ^4He above our detection limit and are free of interference (Tables 1 and 2). The grain size range of this study is similar to that of Heck et al.¹⁵ (Fig. 1). The plots of three grains (A3-01a, A3-01b, and A3-12a) overlap with those of Heck et al. The plots of the other grains in this study are below the detection limit of Heck et al. The percentage of grains with He detected (80 ± 25 (1σ) %; 11 out of 14 examined grains) is higher than the previous studies (<31%)^{15,27–29} because of a lower detection limit in this study (Fig. 1) due to mainly higher ionization efficiency by the strong field ionization³⁰. Indeed, if we remove grains below the detection limit of Heck et al.¹⁵, the percentage (21 ± 12 (1σ) %; 3 out of 14 examined grains; Fig. 1) is similar to each other.

Secondary electron (SE) images of individual SiC grains and their 2-D maps of ^4He , ^{12}C , and ^{28}Si concentrations derived from the 3-D distributions are shown in Fig. 2, panels a, c, d, and b, respectively. Those of SE, ^{28}Si , and ^4He are shown in Fig. 3, panels a, d, g, j, m, and p; b, e, h, k, n, and q; and c, f, i, l, o, and r, respectively. The ^4He content is highly variable between grains ranging from 0.0002 to 0.061 mL g^{-1} (Table 2), e.g., as shown in grains A3-12a (0.059 mL g^{-1}), A3-12b (Low concentration, but not quantifiable due to interference), and A3-12c (0.004 mL g^{-1}) (Fig. 2c). Furthermore, the ^4He content is highly heterogeneous in the depth direction within each grain. The content is high near the surface and rapidly decreases towards the inside, reaching a level below the detection limit at a depth of about 300 nm, e.g., as shown in A3-12a (Figs. 2e–h). The helium concentration near the surface of A3-12a and A3-01a is about 0.02 atomic%, which exceeds the solubility limit in solids. These characteristics suggest that the concentration profile is generated by implantation of high-speed He into the SiC grains.

The primary beam of LIMAS sputtered atoms from grain surfaces. Comparing the SE images before and after sputtering (Fig. 4), it appears that the primary ions sputtered the SiC grains from the surface

Table 2 | ^4He concentration in KJG SiC grain from Murchison

Grain	size / μm	mass [†] /g	bulk ^4He /mL g ⁻¹	bulk ^4He /mL	bulk ^4He /atom	Fluence /mL cm ²	Fluence /atom cm ²	Implantation range /nm	Implantation energy /keV	Distance (1) /ly	Distance (2) /ly	Formation age (1) /My	Formation age (2) /My
A3-01a	2.7	3.32E-11	0.061	2.02E-12	5.44E+07	8.84E-06	2.38E+14	100	15	1.7	0.9	-0.05	-0.03
A3-01b	1.8	9.83E-12	0.030	2.95E-13	7.93E+06	2.90E-06	7.80E+13	50	7	2.9	1.6	-0.09	-0.05
A3-02	2.2	1.79E-11	0.0002	3.59E-15	9.65E+04	2.36E-08	6.35E+11			32.4	17.7	-0.95	-0.52
A3-03	2.2	1.79E-11	0.0007	1.26E-14	3.38E+05	8.26E-08	2.22E+12			17.3	9.5	-0.51	-0.28
A3-04	1.1	2.24E-12	b.d.	b.d.	b.d.	b.d.	b.d.	b.d.	b.d.	b.d.	b.d.	b.d.	b.d.
A3-05	0.9	1.23E-12	0.003	3.69E-15	9.91E+04	1.45E-07	3.90E+12			13.1	7.2	-0.38	-0.21
A3-06	1.1	2.24E-12	0.003	6.73E-15	1.81E+05	1.77E-07	4.76E+12			11.8	6.5	-0.35	-0.19
A3-07	0.6	3.64E-13	0.006	2.18E-15	5.87E+04	1.93E-07	5.20E+12			11.3	6.2	-0.33	-0.18
A3-09a	2.0	1.35E-11	b.d.	b.d.	b.d.	b.d.	b.d.	b.d.	b.d.	b.d.	b.d.	b.d.	b.d.
A3-09b	2.8	3.70E-11	b.d.	b.d.	b.d.	b.d.	b.d.	b.d.	b.d.	b.d.	b.d.	b.d.	b.d.
A3-10	1.6	6.90E-12	0.001	6.90E-15	1.86E+05	8.59E-08	2.31E+12			17.0	9.3	-0.50	-0.27
A3-11	1.5	5.69E-12	0.003	1.71E-14	4.59E+05	2.42E-07	6.50E+12			10.1	5.5	-0.30	-0.16
A3-12a	3.6	7.86E-11	0.059	4.64E-12	1.25E+08	1.14E-05	3.07E+14	100	15	1.5	0.8	-0.04	-0.02
A3-12b	1.8	9.83E-12	*	*	*	*	*	*	*	*	*	*	*
A3-12c	1.8	9.83E-12	0.004	3.93E-14	1.06E+06	3.86E-07	1.04E+13			8.0	4.4	-0.24	-0.13
average	1.8	1.64E-11	0.016	6.41E-13	1.72E+07	2.22E-06	5.98E+13	83	12	11.6	6.3	-0.34	-0.19
median	1.8	9.83E-12	0.003	1.26E-14	3.38E+05	1.93E-07	5.20E+12	100	15	11.3	6.2	-0.33	-0.18
max	3.6	7.86E-11	0.061	4.64E-12	1.25E+08	1.14E-05	3.07E+14	100	15	32.4	17.7	-0.04	-0.02
min	0.6	3.64E-13	0.0002	2.18E-15	5.87E+04	2.36E-08	6.35E+11	50	7	1.5	0.8	-0.95	-0.52

[†]assumed spherical shape. Distance: distance from CSPN under (1) 100 mass%He, 5000 yr; (2) 30 mass%He, 5000 yr. Formation age: anchored by CSPNe phase under (1) and (2). b.d.: below detection limit. *⁴He signals were obscured by intense ⁴He signals from adjacent SiC grains.

almost parallel to the original surface profile. If the sputtering has been carried out to slice through the grain, the He maps should have a He-rich rim around the grain. However, the He maps for each depth layer never show such features, but are homogeneously distributed in each depth layer (Fig. 2e–h). Therefore, He was likely implanted homogeneously over the whole grain surface. The time variation of the noble gas concentration during sputtering from the whole grain area can be regarded as an implantation profile of the SiC grains in the depth direction.

For ^4He detected SiC grains, the depth profiles from the grain surface are shown in Fig. 5. The ^4He signals were detected down to a depth of 300 nm and became background at greater depths. For grains A3-01a, A3-01b, and A3-12a, the ^4He peak appeared at a depth of 100,

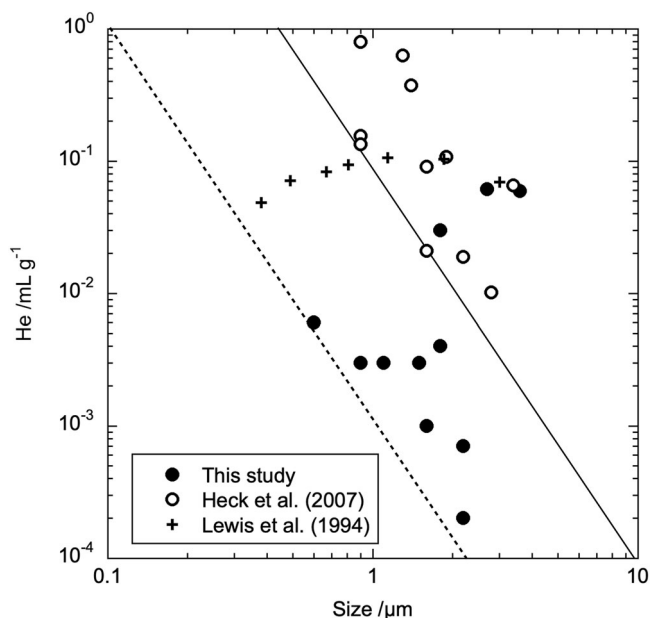


Fig. 1 | ^4He concentrations vs. grain size for mainstream SiC from the Murchison meteorite. Solid line: detection limit of Heck et al. (2007)¹⁵. Dashed line: estimated detection limit of this study. Plots of Heck et al. (2007)¹⁵ (open circle) and this study (solid circle) are analyses of individual grains. Plots of Lewis et al. (1994)⁶ (cross) are bulk analyses of size-sorted SiC grain fractions, not of individual grains. Source data are provided as a Source Data file.

50, and 100 nm, respectively (Fig. 5a). Because implanted He stops at different depths from the material surface corresponding to their kinetic energies, the peaks correspond to the implantation range of $^4\text{He}^{33}$. The implantation ranges at given kinetic energies into SiC were calculated using SRIM software³³ (Supplementary Fig. S1). The kinetic energy can be translated into the velocity of the stellar wind observed in astronomy. The implantation ranges of ^4He for the SiC grains correspond to the kinetic energies of 7–15 keV, corresponding to velocities of 580–850 km s^{-1} for stellar flow, with an average of 12 keV (3 keV/nucleon) (Table 2). The energy range in this study is within the astronomically observed and theoretically estimated ranges of hot stellar wind speeds from CSPNe (about 20 to about 3000 km s^{-1})^{22–26}, and corresponds to stellar temperatures of 30–50 kK. Therefore, it is plausible that the ^4He in the presolar SiC grains is predominantly implanted by the CSPN winds and therefore He-G, supporting the suggestions of previous isotopic studies^{6,15,34}.

In order to simply interpret a relationship between the various size fractions of the SiC grains and their noble gas concentrations among the fractions, an implantation energy of about 50 keV/nucleon has been suggested for the SiC presolar grains¹⁶. This energy is close to the speed of the fastest CSPN wind²⁶. However, the helium implanted in SiC grains with about 50 keV/nucleon (corresponding to a stellar wind speed of about 3000 km s^{-1} and an implantation range of about 700 nm deep) has not been detected in this study. Instead, this study shows that the implantation energies into the SiC grains are variable. This result is robust because the depth profile is directly correlated with the implantation energy, and the SiC grains used in this study were collected from the size-sorted fraction KJG.

The relationships between the grain size of mainstream presolar SiC and its ^4He content (Heck et al.¹⁵ and this study) are compared with those between the size-sorted SiC fraction and its ^4He content (Lewis et al.⁶) (Fig. 1). Large variations of more than two orders of magnitude in He concentration are observed among grains of similar size. Such large variation is consistent with evidence showing that gas-rich grains (about 4% fraction of the SiC in KJG) accounted for more than 90% of the gas concentration measured in aggregates of millions of grains^{27,28}. In laboratory analyses where individual particles were analyzed, a significant number of particles below the detection limit of ^4He were counted; about 70% of the total number of grains analyzed in Heck et al.¹⁵, about 20% in this study. As a result, the values of the size-sorted bulk samples⁶ are plotted on the upper side, and it is difficult to represent implantation energy with a single value. However, this

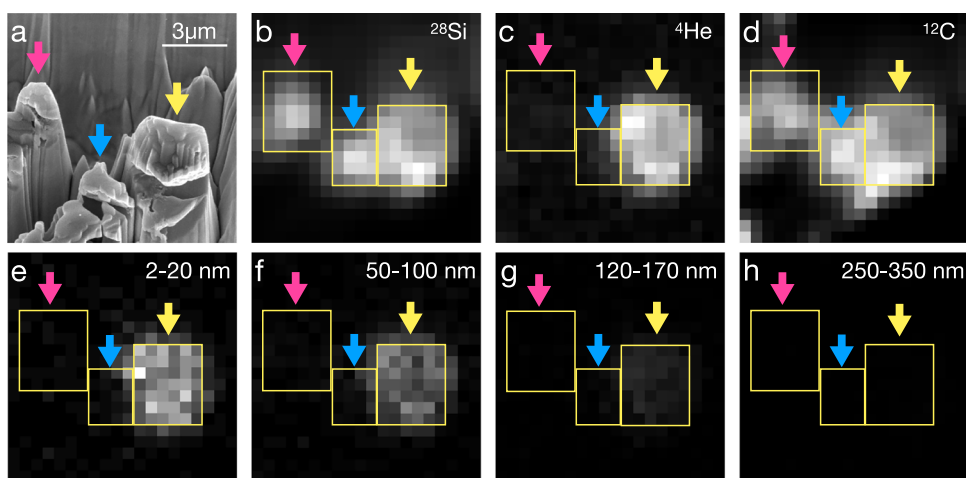


Fig. 2 | Presolar SiC grains A3-12a (yellow arrow), A3-12b (blue arrow), and A3-12c (pink arrow). **a** SE image after measurement. **b** Integrated ^{28}Si image for total measurement depth layers. **c** Integrated ^4He image for total measurement depth layers. **d** Integrated ^{12}C image for total measurement depth layers. **e–h** Averaged

^4He images for measurement depth layers between 2–20, 50–100, 120–170, 250–350 nm, respectively. Grayscale tones in images (e–g) are the same. Yellow rectangles of **b–h** show analyzing areas of depth-profiling. Scale bar is 3 μm for all figures.

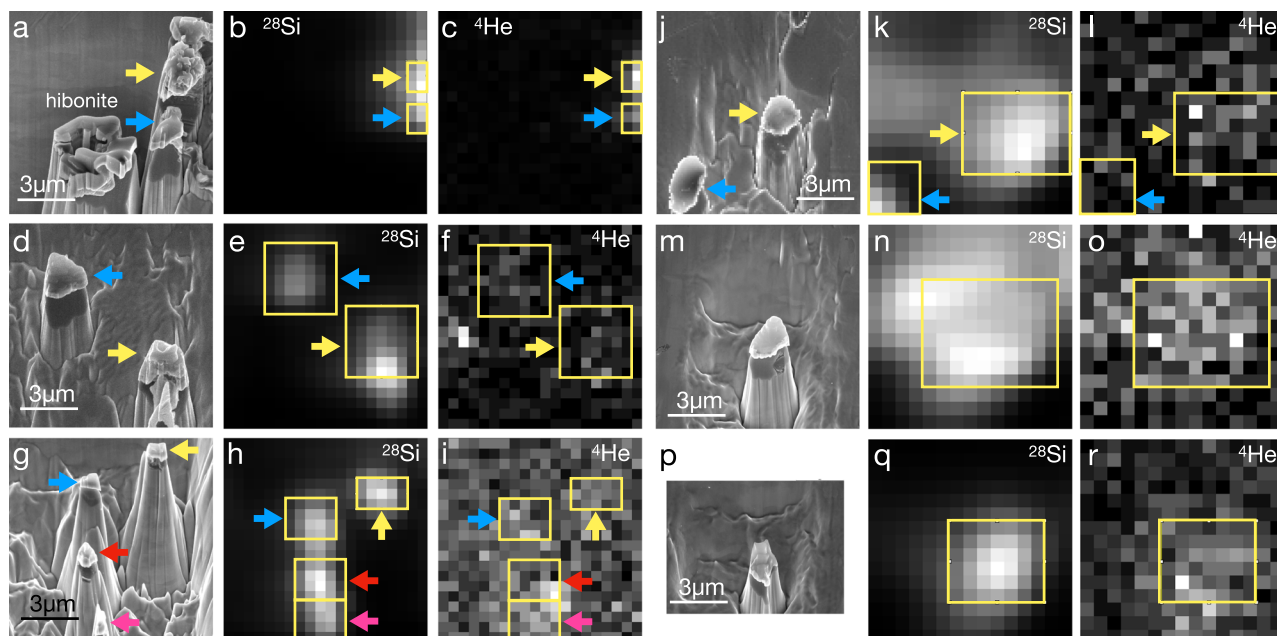


Fig. 3 | Presolar SiC grains. a–c A3-01a (yellow arrow) and A3-01b (blue arrow). **d–f** A3-02 (yellow arrow) and A3-03 (blue arrow). **g–i** A3-04 (yellow arrow), A3-05 (blue arrow), A3-06 (red arrow), A3-07 (pink arrow). **j–l** A3-09a (yellow arrow), and A3-09b (blue arrow). **(m–o)** A3-10. **p–r** A3-11. **a, d, g, j, p** SE image after

measurement. **b, e, h, k, q)** Integrated ^{28}Si image for total measurement depth layers. **(c, f, i, l, r)** Integrated ^4He image for total measurement depth layers. Yellow rectangles show analyzing areas of depth-profiling. Scale bar is $3\ \mu\text{m}$ for all figures.

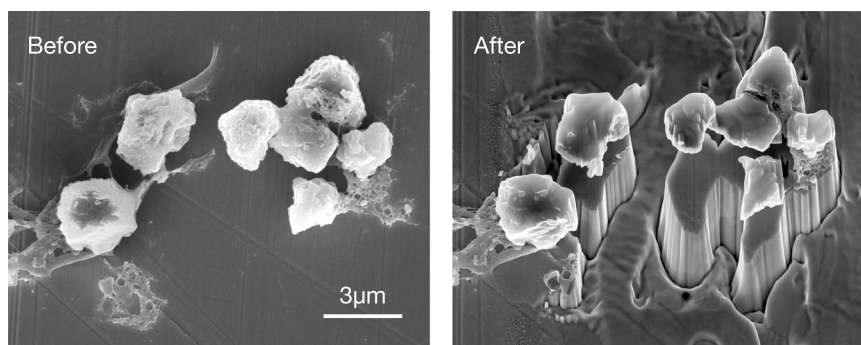


Fig. 4 | SE image of presolar SiC grains before and after sputtering by LIMAS. Sputtering layer thickness is estimated to be 570 nm on the SiC grains. Sputtering rate is faster for Au substrate than for SiC. The sputtering of SiC grains occurred almost parallel to the original surface profile.

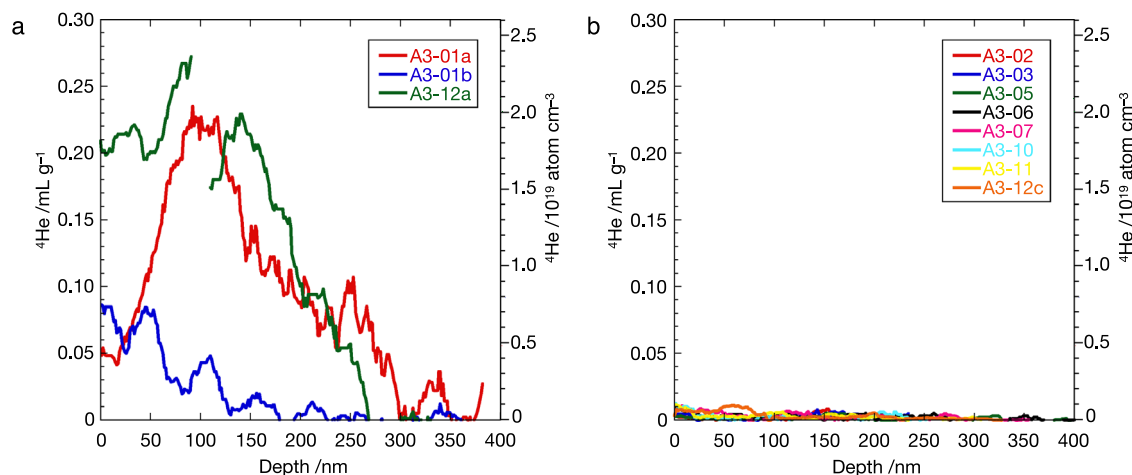


Fig. 5 | Depth profiles of ^4He into presolar SiC grains. a Grains with high ^4He contents. A3-01a (red), A3-01b (blue), and A3-12a (green). **b** Grains with low ^4He contents. A3-02 (red), A3-03 (blue), A3-05 (green), A3-06 (black), A3-07 (pink), A3-10 (light blue), A3-11 (yellow), and A3-12c (orange). The individual depth profiles for

each grain can be found in Supplementary Figs. S2–S9. The jagged wiggles in the curves are measurement uncertainties caused by instrumental instabilities. Source data are provided as a Source Data file.

discussion cannot rule out the existence of SiC grains that have been implanted with He at high energies, such as about 50 keV/nucleon. For example, such high implantation energy travels implanted ^4He a great distance of about $1\ \mu\text{m}$ and stops. If this implantation occurred for $1\text{-}\mu\text{m}$ -sized SiC grains, the helium would stop near the grain surface on the opposite side of the implantation. We have depth profiling results from three SiC grains (A3-05, A3-06, and A3-07) that are $1\ \mu\text{m}$ or slightly smaller in size and may be applicable in this case (Fig. 5b). However, it is strange that such high-energy implantations have not been observed for larger SiC grains. Further study is required to investigate the real distribution of the implantation energy into SiC grains for more precise discussions.

Artificial peak broadening would have occurred because the sputtering was not exactly parallel to the original surface profiles due to the surface irregularities of each grain. Therefore, it is difficult to assign ^4He peaks for grains with low ^4He concentrations even if they also have ^4He peaks at a depth of 50–100 nm. In the results, for other grains, weak ^4He signals appeared at depths shallower than 300 nm with no clear peaks (Fig. 5b).

On the other hand, stellar wind velocities for AGB stars are less than $40\ \text{km s}^{-1}$ ^{18–21}. The kinetic energy of the AGB ^4He wind is calculated to be less than 0.05 keV, and the implantation range into SiC is less than 1 nm (Supplementary Fig. S1), which is much smaller than the depth resolution of the LIMAS analysis. Therefore, the ^4He signal at the grain surface would be mainly contributed by the He-G, but might be due to a small contribution of implanted thermal and suprathermal components of the AGB stellar winds. This also corroborates previous isotopic studies^{6,15} that concluded the He-G component comprised over 95% of the measured stellar gas in mainstream SiC grains.

History of presolar SiC formation

The fluences of the presolar SiC grains calculated from the depth profiles are variable, ranging from 6.4×10^{11} to $3.1 \times 10^{14}\ ^4\text{He cm}^{-2}$ (Table 2). Typical mass-loss rate of CSPNe for 30–50 kK is about $5 \times 10^{-9}\ M_{\odot}\ \text{y}^{-1}$ ^{22–24,35,3}, and the typical period of CSPNe is about 5000 y¹⁷. The He implantation into the presolar grain was continued during this period. The chemical composition of CSPN wind is very diverse, ranging from H-deficient (He-rich) to H-rich (solar-like)¹⁷. We therefore performed our calculations assuming two endmembers: one with a 100 mass% proportion of He in the total mass-loss atoms (He-rich) and one with a 30 mass% proportion (solar-like). The latter is derived from the solar abundance³⁷. Using the ^4He fluences in this study and these two endmembers, the sites of presolar SiC grains at the end of the CSPNe phase, where noble gas was implanted, are calculated to be 0.8–32 ly from the CSPNe (Table 2 and see methods, subsection ‘CSPN wind irradiation and formation age of SiC’ for details). The sites for SiC grains of top three fluences (Fig. 5a), distances of 0.8–2.9 ly from the CSPNe, are roughly consistent with the radii of planetary nebulae in the Galaxy (less than 5 ly for the vast majority³⁸), e.g., Ring Nebula (M57) and Helix Nebula (NGC 7293)^{39,40}, suggesting that the implantation events occurred in planetary nebulae.

Since the grains in the circumstellar envelopes and the planetary nebulae expand with the gas, the time periods that the grains have moved from the formation site, which is close to the AGB star, to the site at the end of the CSPNe phase can be calculated using the expansion velocity of the circumstellar envelope (see methods, subsection ‘CSPN wind irradiation and formation age of SiC’ for details). We refer to this period as the formation age of the presolar SiC grains anchored by the CSPNe phase of stellar evolution, i.e., time = 0 is at the end of the CSPNe phase. We also applied this method to calculate the formation ages of the mainstream SiC grains measured by Heck et al.¹⁵. The formation ages of the mainstream SiC grains (Tables 2 and 3) are spread over the last about 1 My period of the AGB star phase of stellar evolution (Fig. 6). A closer inspection shows that the Murray grains¹⁵ formed at the very end of the AGB phase followed by the Murchison

grains by the same authors¹⁵. Some of our Murchison grains also formed at the end of the AGB phase, but other grains formed much earlier in the AGB phase (Fig. 6). The locations of the noble gas implantation sites for individual SiC grains and their formation ages are derived in the case of typical CSPNe and AGB stars. Since the parameters are variable among individual CSPNe and the stellar evolution stages, the relative errors are estimated to be approximately 100% for the implantation sites and the formation ages, with a minimum resolution of about 0.5 ly for the site and 5 ky for the age (see methods, subsection ‘CSPN wind irradiation and formation age of SiC’ for details).

This argument of formation ages derived from the noble gas data is also consistent with the $^{12}\text{C}/^{13}\text{C}$ ratios of the presolar grains. The $^{12}\text{C}/^{13}\text{C}$ ratios are in the range of 10–35 for the O-rich envelopes of AGB stars, while they are ~25–90 for the C-rich envelopes^{41,42}. Due to the ^{12}C that is dredged-up during the AGB phase, the $^{12}\text{C}/^{13}\text{C}$ ratio of the envelope increases as a star evolves¹⁷. In general, the grains with higher $^{12}\text{C}/^{13}\text{C}$ ratios formed in the later stage of the AGB phase than those with lower $^{12}\text{C}/^{13}\text{C}$ ratios. The mean isotopic ratios of the Murchison grains in this study, the Murchison grains of Heck et al.¹⁵, and the Murray grains¹⁵ is 40.5 (Table 1), 60.0 (Tables 3), and 65.8 (Table 3), respectively. Changes in these three $^{12}\text{C}/^{13}\text{C}$ ratios would be related to the stellar evolution of AGB stars in this order. Therefore, the formation ages of the three sets of grains derived from their noble gas data are consistent with the scenario inferred from the $^{12}\text{C}/^{13}\text{C}$ ratios of the grains, indicating that our methods and conclusions are valid.

The stellar wind evidence obtained in this study reveals the formation history of individual mainstream SiC grains. AGB stars appear to have continued to form SiC grains at least during their late stages. We found evidence that the helium in the presolar SiC grains was from the CSPN hot winds. The sites where the CSPN hot wind implantation has occurred range from 0.3 to 32 ly from the center of the planetary nebula, corresponding to the formation ages ranging from 0.95 to 0.01 My before the end of CSPNe. The derived new approach can also be applied to all presolar grains other than SiC, shedding light on the origin and history of circumstellar dusts formed by various types of stars.

Methods

Sample and sample preparation

The SiC grains used in this study were extracted from the Murchison meteorite (CM2). A detailed separation procedure is described by Amari et al.³². We briefly summarize it here. Starting with about 80 g of the Murchison meteorite, silicates were first dissolved using HF. Sulfur was removed with CS_2 and KOH. After nanodiamonds were extracted, the remaining residue was oxidized with $\text{Na}_2\text{Cr}_2\text{O}_7$ to remove reactive kerogen. Density separation was performed on the residue using sodium polytungstate [$\text{Na}_6(\text{H}_2\text{W}_{12}\text{O}_{40})$] to yield several density fractions. The heaviest density fraction ($>2.3\ \text{g/cm}^3$) was heated with perchloric acid (HClO_4) to destroy remaining organic matter. Then, it was heated with concentrated sulfuric acid (H_2SO_4) to remove spinel (MgAl_2O_4). The residue was then separated by size into nine SiC-rich fractions (KJA – KJI) by centrifugation. The nominal size range of the KJG was 1.5–3 μm . The observed range from 46 SiC grains was 2.1–4.5 μm with the average diameter of 3.0 μm . Silicon carbide grains comprised 73% of the KJG grains. The rest were comprised of hibonite (CaAl_2O_9), corundum (Al_2O_3), and other phases.

For this study, the KJG grains were suspended in a 4:1 mixture of iso-propanol and H_2O and were deposited onto a gold plate as a droplet. The droplet was dried, and the SiC grains in the droplet remained on the surface of the plate. We analyzed the samples to identify mineral phases and the shapes before and after 3-D helium analysis using a field-emission scanning electron microscope (FE-SEM) (JEOL JSM-7000F) equipped with an energy-dispersive X-ray (EDS) spectroscopic detector (Oxford X-Max 150) at Hokkaido University. Images of

Table 3 | ⁴He concentration of mainstream SiC grain from Murchison and Murray (after Heck et al.¹⁵, 2007)

Grain	size/ μm	mass/g	bulk ⁴ He /mL g ⁻¹	bulk ⁴ He /mL ⁴ He /mL	bulk ⁴ He /atom	Fluence /mL cm ²	Fluence /atom cm ²	Distance (1) /ly	Distance (2) /ly	Formation age (1) /My	Formation age (2) /My	¹³ C/ ¹² C
Murchison												
SiC102	1.3	3.70E-12	0.6281	2.33E-12	6.26E+07	4.38E-05	1.18E+15	0.8	0.4	-0.02	-0.01	72.7
SiC128	0.9	1.23E-12	0.796	9.78E-13	2.63E+07	3.84E-05	1.03E+15	0.8	0.4	-0.02	-0.01	47.0
SiC138	1.6	6.90E-12	0.0903	6.23E-13	1.68E+07	7.75E-06	2.09E+14	1.8	1.0	-0.05	-0.03	51.3
SiC166	1.4	4.62E-12	0.3732	1.73E-12	4.64E+07	2.80E-05	7.54E+14	0.9	0.5	-0.03	-0.02	60.9
SiC014	3.4	6.62E-11	0.0655	4.34E-12	1.17E+08	1.20E-05	3.21E+14	1.4	0.8	-0.04	-0.02	90.0
SiC068	2.8	3.70E-11	0.0101	3.74E-13	1.01E+07	1.52E-06	4.08E+13	4.0	2.2	-0.12	-0.06	56.4
SiC087	0.9	1.23E-12	0.154	1.89E-13	5.09E+06	7.44E-06	2.00E+14	1.8	1.0	-0.05	-0.03	19.3
SiC105	2.2	1.79E-11	0.0188	3.37E-13	9.07E+06	2.22E-06	5.97E+13	3.3	1.8	-0.10	-0.05	57.7
SiC110	1.9	1.16E-11	0.1069	1.24E-12	3.32E+07	1.09E-05	2.93E+14	1.5	0.8	-0.04	-0.02	67.7
SiC121	1.6	6.90E-12	0.0209	1.44E-13	3.88E+06	1.79E-06	4.83E+13	3.7	2.0	-0.11	-0.06	67.4
SiC134	0.9	1.23E-12	0.134	1.65E-13	4.43E+06	6.47E-06	1.74E+14	2.0	1.1	-0.06	-0.03	69.4
average	1.7	1.44E-11	0.218	1.13E-12	3.04E+07	1.46E-05	3.92E+14	2.0	1.1	-0.06	-0.03	60.0
median	1.6	6.90E-12	0.107	6.23E-13	1.68E+07	7.75E-06	2.09E+14	1.8	1.0	-0.05	-0.03	60.9
max	3.4	6.62E-11	0.796	4.34E-12	1.17E+08	4.38E-05	1.18E+15	4.0	2.2	-0.02	-0.01	90.0
min	0.9	1.23E-12	0.0101	1.44E-13	3.88E+06	1.52E-06	4.08E+13	0.8	0.4	-0.12	-0.06	19.3
Murray												
SiC207	1	1.69E-12	1.036	1.75E-12	4.70E+07	5.56E-05	1.50E+15	0.7	0.4	-0.02	-0.01	58.0
SiC210	1.4	4.62E-12	1.065	4.92E-12	1.32E+08	8.00E-05	2.15E+15	0.6	0.3	-0.02	-0.01	70.7
SiC211	1.1	2.24E-12	0.346	7.76E-13	2.09E+07	2.04E-05	5.49E+14	1.1	0.6	-0.03	-0.02	59.2
SiC219	1.1	2.24E-12	0.536	1.20E-12	3.23E+07	3.16E-05	8.51E+14	0.9	0.5	-0.03	-0.01	85.9
SiC242	0.8	8.63E-13	1.144	9.87E-13	2.66E+07	4.91E-05	1.32E+15	0.7	0.4	-0.02	-0.01	39.6
SiC252	1	1.69E-12	0.828	1.40E-12	3.75E+07	4.44E-05	1.20E+15	0.7	0.4	-0.02	-0.01	69.3
SiC271	0.6	3.64E-13	2.049	7.46E-13	2.01E+07	6.60E-05	1.77E+15	0.6	0.3	-0.02	-0.01	78.4
SiC215	0.7	5.78E-13	1.403	8.11E-13	2.18E+07	5.27E-05	1.42E+15	0.7	0.4	-0.02	-0.01	101.6
SiC228	0.8	8.63E-13	1.062	9.16E-13	2.46E+07	4.56E-05	1.23E+15	0.7	0.4	-0.02	-0.01	58.4
SiC229	1.1	2.24E-12	0.354	7.94E-13	2.14E+07	2.09E-05	5.62E+14	1.1	0.6	-0.03	-0.02	54.7
SiC235	0.8	8.63E-13	1.342	1.16E-12	3.11E+07	5.76E-05	1.55E+15	0.7	0.4	-0.02	-0.01	53.2
SiC247	0.8	8.63E-13	1.015	8.76E-13	2.36E+07	4.36E-05	1.17E+15	0.8	0.4	-0.02	-0.01	60.0
Average	0.9	1.59E-12	1.015	1.36E-12	3.66E+07	4.73E-05	1.27E+15	0.8	0.4	-0.02	-0.01	65.8
Median	0.9	1.27E-12	1.049	9.52E-13	2.56E+07	4.74E-05	1.27E+15	0.7	0.4	-0.02	-0.01	59.6
Max	1.4	4.62E-12	2.049	4.92E-12	1.32E+08	8.00E-05	2.15E+15	1.1	0.6	-0.02	-0.01	101.6
Min	0.6	3.64E-13	0.3460	7.46E-13	2.01E+07	2.04E-05	5.49E+14	0.6	0.3	-0.03	-0.02	39.6

*assumed spherical shape. Distance: distance from CSPN under (1) 100 mass%He, 5000 yr. (2) 30 mass%He, 5000 yr. Formation age: anchored by CSPNe phase under (1) and (2).

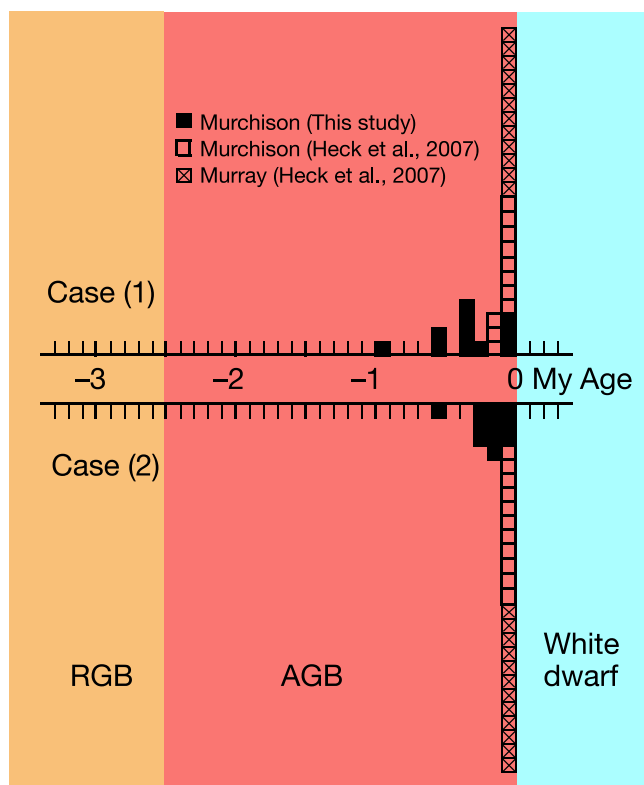


Fig. 6 | Histogram of formation age of mainstream presolar SiC grains. The age=0 is anchored by the CSPNe phase of stellar evolution. The SiC grains continued to form during the last 1 My period of the AGB star phase of stellar evolution. The periods of stellar evolutionary phases are from Herwig (2005)¹⁷. Data from Tables 2 and 3 are plotted. Solid square (from Murchison of this study), open square (from Murchison of Heck et al.¹⁵, 2007), and crossed square (from Murray of Heck et al.¹⁵, 2007). Case (1): 100 mass% He flux during 5000 yr; Case (2): 30 mass% He flux during 5000 yr.

secondary electron (SE), back scattered electron (BSE), and elements were observed at 15 kV acceleration voltage and about 30 nA beam current.

3-D helium analysis by LIMAS

Following the same protocol of ref. 43, here we measured the 3-D analysis of SiC grains by a secondary neutral mass spectrometer (JEOL LIMAS) at Hokkaido University³⁰. The three-dimensional distribution of $^4\text{He}^+$, $^{12,13}\text{C}^+$ or $^{12,13}\text{C}^{2+}$, and $^{28,29,30}\text{Si}^{2+}$ or $^{28,29,30}\text{Si}^{4+}$ was obtained from the surface layer of SiC grains. A pulsed primary beam of $^{69}\text{Ga}^+$ (30 keV, 30 nA) was focused to a spot of 1 μm in diameter on the sample surface with the pulse period of 400 ns. Sputtered secondary neutrals were ionized by a focused (30 μm in diameter) femtosecond laser beam at 50 μm above the sputtering points under a strong-field ionization condition. The laser pulse was 35 fs with an energy of 5.5 mJ and 1 kHz repetition using the Coherent Astrella. The vacuum in the sample chamber was maintained at 4×10^{-9} Pa during the measurement. Under similar conditions, about 70% of ^4He atoms (about 70%) are ionized⁴⁴. Positive ions were introduced into a multi-turn time-of-flight mass spectrometer (MULTUM II) by an acceleration voltage of -5 kV with 1 kHz repetition, which is synchronized with the primary beam pulses⁴⁵. The flight path length in the mass spectrometer was set to 219 m for $^4\text{He}^+$, yielding a mass resolving power of $M/\Delta M$ (FWHM) of about 13,000 (Fig. 7). The ion signals from 100 mass scans were accumulated at each spot. The details for ion detection and data processing are reported by Bajo et al.⁴⁶.

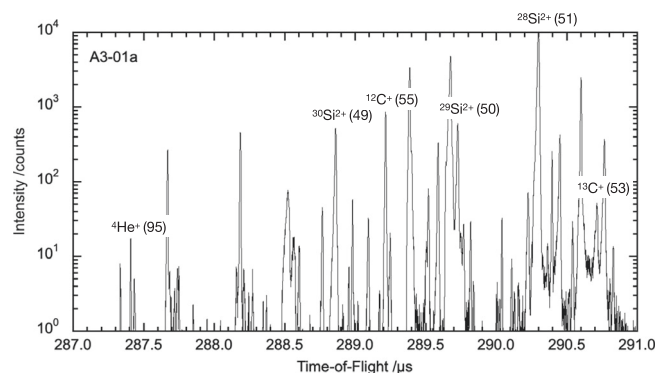


Fig. 7 | Time-of-flight spectrum of presolar grain A3-01a. Data of depth layers from 30 to 150 nm are integrated. Multi-turn number for each isotope peak is given in parentheses. Source data are provided as a Source Data file.

The primary beam was scanned with 500 nm and 880 nm step intervals in the x- and y-directions, respectively, to obtain a selected rectangular area of the sample. The difference in the step intervals is due to the incident angle of the primary beam was set to 55 degrees⁴⁷. Here, we define a rectangle image as one depth layer. To obtain three-dimensional distributions of the measured isotopes, we repeated the measurements of the depth layers until the ^4He signals from SiC grains reached the background level. Because the SiC grains were sparsely aggregated on the gold plate, the selected area contained several SiC grains (e.g., Fig. 2). From the data of the selected area, we selected an appropriate pixel area (yellow rectangles of Figs. 2 and 3) to cover individual single SiC grains to obtain 3-D maps for each grain. It appeared that the primary ions sputtered the SiC grains from the surface almost parallel to the original surface profile (see text). Therefore, the depth layers of the 3-D map were parallel to the original surface. The time variation of an isotope intensity of each depth layer for a given grain can be regarded as a depth profile from the surface. However, since the sputtering is not perfectly parallel to the original surface profile and the surface is not smooth, peak broadening would have occurred artificially for the implantation profiles. Depth profiling of $^4\text{He}^+$, $^{12,13}\text{C}^+$ or $^{12,13}\text{C}^{2+}$, and $^{28,29,30}\text{Si}^{2+}$ or $^{28,29,30}\text{Si}^{4+}$ intensities for each grain is shown in Supplementary Figs. S2–S9.

The isotope ratio of $^{12}\text{C}/^{13}\text{C}$ was calculated from the intensity ratio of the depth profiles for each grain. Instrumental reproducibility and mass fractionation were evaluated using a standard of ^4He -implanted SiC wafer, assuming the standard to have a terrestrial $^{12}\text{C}/^{13}\text{C}$ ratio. The reproducibility and uncertainty of the fractionation were both about 100% and are similar to the standard deviations shown in Table 1. We also calculated the $^{29}\text{Si}/^{28}\text{Si}$ and $^{30}\text{Si}/^{28}\text{Si}$ ratios using the same procedures as for the $^{12}\text{C}/^{13}\text{C}$ ratio. The reproducibility is also about 100%. As a result, the Si isotopic compositions of all the SiC grains are indistinguishable from the solar ratios.

Following the same protocol as ref. 43, here the $^4\text{He}^+$ intensities normalized to the $^{12}\text{C}^+$ or $^{12}\text{C}^{2+}$ intensities were used to calculate ^4He concentrations using relative sensitivity factors (RSFs). The RSFs and sputtering rates were determined by measurements of two standards of ^4He -implanted SiC wafers under the same analytical conditions before each analysis. The implanted fluence and energy of ^4He were 1×10^{15} atoms cm^{-2} and 30 keV for the first standard, and 2×10^{15} atoms cm^{-2} and 20 keV for the second standard. The depths of sputtered craters on the standard were measured by a laser microscope (Keyence VK-X200). A typical depth profile of the standard is shown in Supplementary Fig. S10. After each analysis, background measurements for the ^4He , which signal come from residual ^4He in the sample chamber vacuum, were performed without primary beam irradiation. The RSFs

and ${}^4\text{He}$ concentrations were calculated by the following equations:

$$RSF = \frac{\Phi \times n}{\sum \left\{ (I_{4\text{He}} - I_{4\text{He}}^{\text{BG}}) / I_{12\text{C}} \right\}_{\text{std}} \times d} \quad (1)$$

$$[{}^4\text{He}] = RSF \times (I_{4\text{He}} / I_{12\text{C}}) \quad (2)$$

where std denotes standard analysis, Φ is a fluence of implanted ${}^4\text{He}$ (atoms cm^{-2}), $I_{4\text{He}}$ and $I_{12\text{C}}$ are signal intensities of ${}^4\text{He}^+$ and ${}^{12}\text{C}^+$ or ${}^{12}\text{C}^{2+}$, $I_{4\text{He}}^{\text{BG}}$ is a mean background intensity of ${}^4\text{He}^+$ for the depth profiling, n is total depth layers, d is a sputtered crater depth (cm) at n , and $[{}^4\text{He}]$ is an atomic concentration of ${}^4\text{He}$ (atoms cm^{-3}). The error (standard deviation) of the RSF value applied to each sample measurement are estimated to be about 20%.

We exclude grains containing ${}^4\text{He}$ below the detection limit of this study. We define the detection limit as signal ratios of total ${}^4\text{He}$ of a grain to background equal to or less than 3 (3σ criterion). The background signal was measured at the gold plate area close to each SiC grain. We also exclude grains that were obscured by intense ${}^4\text{He}$ signals from adjacent SiC grains (Table 1).

Since the ${}^4\text{He}$ signals were weak and therefore noisy, we evaluated a moving smoothed mean of the profile (Supplementary Figs. S2–S9). We employed 21 points, equivalent to about 30 nm, to smooth the profiles. The smoothed depth profiles are compiled in Fig. 5. Assuming that the grains are spherical, and that the implantation occurred isotropically, we calculate the bulk ${}^4\text{He}$ composition, the bulk ${}^4\text{He}$ numbers, and the fluence of each grain from the depth profiles (Table 2).

CSPN wind irradiation and formation age of SiC

When a solar mass normalized mass-loss rate of CSPN \dot{M}_{CSPN} is observed, the mass-loss rate of He \dot{M}_{He} is derived as

$$\dot{M}_{\text{He}} = \alpha \dot{M}_{\text{CSPN}} M_{\odot} / m_{\text{He}} \quad (3)$$

where α , M_{\odot} , and m_{He} are He proportion of total mass-loss atoms, solar mass, and mass of He, respectively. Assuming isotropic mass-loss, the He fluence Φ_{He} into a presolar SiC grain is given as

$$\Phi_{\text{He}} = (\dot{M}_{\text{He}} \Delta t) / (4\pi r^2) \quad (4)$$

where Δt and r are the duration time of the CSPN wind irradiation and distance from the CSPN, respectively. By entering the period of the CSPN phase in Δt , we can derive the distance r_{imp} at the end of the CSPN phase.

The Φ_{He} for each SiC grain was calculated from the depth profiles measured in this study and from the concentration and the grain size in the previous study¹⁵ (Tables 2 and 3). The \dot{M}_{CSPN} is astronomically observed by the previous studies^{22–24,35,36}. The range of the \dot{M}_{CSPN} by astronomical observations is $1\text{--}30 \times 10^{-9} M_{\odot} \text{y}^{-1}$ for the stellar temperature of 30–50 kK, with the median being $4.5 \times 10^{-9} M_{\odot} \text{y}^{-1}$ ^{23,35,36}. On the other hand, the \dot{M}_{CSPN} by numerical simulations for the stellar temperature of 30–50 kK is $8.5 \pm 3.8 \times 10^{-9} M_{\odot} \text{y}^{-1}$ ²⁴, and $4.3 \pm 1.5 \times 10^{-9} M_{\odot} \text{y}^{-1}$ ²². The relative errors of the \dot{M}_{CSPN} for the numerical simulations are similar to each other at around 40%. Due to the poorly known distances to CSPNe and other observational difficulties, which may introduce the large variations of \dot{M}_{CSPN} ²², we adopted a 40% uncertainty in \dot{M}_{CSPN} . Due to the potential overestimation of \dot{M}_{CSPN} predicted by Pauldrach et al.²², as well as the agreement between the observational material value and the prediction by Kr̄t̄icka et al., we adopted $5 \pm 2 \times 10^{-9} M_{\odot} \text{y}^{-1}$ for \dot{M}_{CSPN} . The evolutive age of CSPNe for 30–50 kK is $5 \pm 5 \text{ky}$ ⁴⁸ and the period of the typical CSPN phase is about 5 ky¹⁷. We adopted $5 \pm 5 \text{ky}$ for Δt . We used the values of $5 \times 10^{-9} M_{\odot} \text{y}^{-1}$ for \dot{M}_{CSPN} and 5000 y for Δt to calculate r_{imp} (Tables 2 and 3).

Since the grains were formed around the AGB stars^{11,49}, and was carried outwards by radiation pressure, reaching higher distances⁵⁰, the grains in the circumstellar envelopes of the AGB stars expand with the gas, the formation age of the mainstream SiC grains anchored by the end of CSPNe phase t_{F} is calculated as

$$t_{\text{F}} = -r_{\text{imp}} / \nu \quad (5)$$

where ν is expansion velocity of circumstellar envelope of AGB star. The ν ranges from 5 to 30 km s^{-1} ⁵¹ and the typical value is 10.2 ± 5.3 (1σ) km s^{-1} ^{42,52,53} because the variations of ν depend on stellar mass and chemical composition^{18,54}. In addition, the ν would be accelerated to 25 km s^{-1} in the planetary nebula phase by the fast CSPN wind^{55,56}. The distance of the SiC migration in the planetary nebula phase would be calculated to be about 0.4 ly based on the period of the typical CSPN phase of 5 ky. This means that the resolution for r_{imp} and t_{F} is about 0.5 ly and about 5 ky, respectively. We used the value of 10 km s^{-1} for ν to calculate t_{F} (Tables 2 and 3).

We calculated r_{imp} and t_{F} using the typical values for CSPNe in Tables 2 and 3. However, since the typical values include the aforementioned uncertainties, it is necessary to evaluate the accuracy of the individual calculation results. The uncertainties for the parameters are summarized as follows: $\dot{M}_{\text{CSPN}} = 5 \pm 2 \times 10^{-9} M_{\odot} \text{y}^{-1}$, $\Delta t = 5 \pm 5 \text{ky}$, and $\nu = 10 \pm 5.3 \text{km s}^{-1}$. Therefore, the calculation results are primarily influenced by the uncertainty of Δt . Assuming the errors are independent of each other, the relative error of r_{imp} is calculated to be 110% from Eqs. 3 and 4, and the relative error of t_{F} is calculated to be 120% from Eq. 5. Additionally, the minimum accuracies of r_{imp} and t_{F} are estimated to be about 0.5 ly and about 5 ky, respectively.

Data availability

The data supporting the main findings of this study are available in the paper, its Supplementary Information, and Source Data files. The data used for the Supplementary Information are available at <https://doi.org/10.6084/m9.figshare.29827193>. The analyzed parts of the samples are destroyed by sputtering. Source data are provided with this paper.

References

- Zinner E. 1.4 - Presolar Grains. In: *Treatise on Geochemistry (Second Edition)* (eds Holland H. D., Turekian KK). Elsevier (2014).
- Bernatowicz, T. et al. Evidence for interstellar SiC in the Murray carbonaceous meteorite. *Nature* **330**, 728–730 (1987).
- Tang, M. & Anders, E. Isotopic anomalies of Ne, Xe, and C in meteorites. II. Interstellar diamond and SiC: Carriers of exotic noble gases. *Geochim Cosmochim. Acta* **52**, 1235–1244 (1988).
- Prombo, C. A., Podosek, F. A., Amari, S. & Lewis, R. S. s-process Ba isotopic compositions in presolar SiC from the Murchison meteorite. *Astrophys J.* **410**, 393–399 (1993).
- Hoppe, P., Amari, S., Zinner, E., Ireland, T. & Lewis, R. S. Carbon, nitrogen, magnesium, silicon, and titanium Isotopic compositions of single interstellar silicon carbide grains from the Murchison carbonaceous chondrite. *Astrophys. J.* **430**, 870–890 (1994).
- Lewis, R. S., Amari, S. & Anders, E. Interstellar grains in meteorites: II. SiC and its noble gases. *Geochim. Cosmochim. Acta* **58**, 471–494 (1994).
- Podosek, F. A., Prombo, C. A., Amari, S. & Lewis, R. S. s-process Sr isotopic compositions in presolar SiC from the Murchison meteorite. *Astrophys. J.* **605**, 960–965 (2004).
- Lugaro, M. et al. Origin of Large Meteoritic SiC Stardust Grains in Metal-rich AGB Stars. *Astrophys J.* **898**, 96 (2020).
- Cristallo, S. et al. Mass and metallicity distribution of parent AGB stars of presolar SiC. *Astron. Astrophys.* **644**, A8 (2020).
- Kobayashi, C., Karakas, A. I. & Lugaro, M. The origin of elements from carbon to uranium. *Astrophys. J.* **900**, 179 (2020).

11. Yasuda, Y. & Kozasa, T. Formation of SiC grains in pulsation-enhanced dust-driven wind around carbon-rich asymptotic giant branch stars. *Astrophys. J.* **745**, 159 (2012).
12. Heck, P. R. et al. Lifetimes of interstellar dust from cosmic ray exposure ages of presolar silicon carbide. *Proc. Natl. Acad. Sci.* **117**, 1884 (2020).
13. Gyngard, F., Amari, S., Zinner, E. & Ott, U. Interstellar exposure ages of large presolar SiC grains from the Murchison meteorite. *Astrophys. J.* **694**, 359 (2009).
14. Heck, P. R. et al. Interstellar residence times of presolar SiC dust grains from the Murchison carbonaceous meteorite. *Astrophys. J.* **698**, 1155–1164 (2009).
15. Heck, P. R. et al. Presolar He and Ne isotopes in single circumstellar SiC grains. *Astrophys. J.* **656**, 1208–1222 (2007).
16. Verchovsky, A. B., Wright, I. P. & Pillinger, C. T. Astrophysical Significance Of Asymptotic Giant Branch Stellar Wind Energies Recorded In Meteoritic SiC Grains. *Astrophys. J.* **607**, 611–619 (2004).
17. Herwig, F. Evolution of Asymptotic Giant Branch Stars. *Annu. Rev. Astron. Astrophys.* **43**, 435–479 (2005).
18. Bladh, S., Eriksson, K., Marigo, P., Liljegren, S. & Aringer, B. Carbon star wind models at solar and sub-solar metallicities: a comparative study. *AA* **623**, A119 (2019).
19. Schöier, F. L. & Olofsson, H. Models of circumstellar molecular radio line emission. *AA* **368**, 969–993 (2001).
20. Ramstedt, S. & Olofsson, H. The $^{12}\text{CO}/^{13}\text{CO}$ ratio in AGB stars of different chemical type. *AA* **566**, A145 (2014).
21. Groenewegen, M. A. T. et al. The ALMA detection of CO rotational line emission in AGB stars in the Large Magellanic Cloud. *AA* **596**, A50 (2016).
22. Krtićka, J., Kubát, J. & Krtićková, I. Stellar wind models of central stars of planetary nebulae. *Astron. Astrophys.* **635**, A173 (2020).
23. Herald, J. E. & Bianchi, L. The winds of hydrogen-rich central stars of planetary nebulae. *Mon. Not. R. Astron. Soc.* **417**, 2440–2464 (2011).
24. Pauldrach, A. W. A., Hoffmann, T. L. & Méndez, R. H. Radiation-driven winds of hot luminous stars - XV. Constraints on the mass–luminosity relation of central stars of planetary nebulae. *AA* **419**, 1111–1122 (2004).
25. Volk, K. & Kwok, S. Dynamical evolution of planetary nebulae. *Astron. Astrophys.* **153**, 79–90 (1985).
26. Iben, I. Planetary nebulae and their central stars — origin and evolution. *Phys. Rep.* **250**, 1–94 (1995).
27. Nichols, R. H. Jr., Hohenberg, C. M., Hoppe, P., Amari, S. & Lewis, R. S. $^{22}\text{Ne-E(H)}$ and ^4He in single SiC and $^{22}\text{Ne-E(L)}$ in single C of known C-isotopic compositions. *Lunar Planet. Sci. Conf.* **23**, 989 (1992).
28. Nichols, R. H. Jr., Hohenberg, C. M., Amari, S. & Lewis, R. S. $^{22}\text{Ne-E(H)}$ and ^4He measured in individual SiC grains using laser gas extraction. *Meteoritics* **26**, 377–378 (1991).
29. Nichols, R. H. Jr., Amari, S., Hoppe, P. & LR, S. $^{20,22}\text{Ne-E(H)}$ and ^4He measured in single interstellar SiC grains of known C-isotopic composition. *Meteoritics* **28**, 410–411 (1993).
30. Bajo, K. -i & Yurimoto, H. Nanoscale analysis of noble gas in solids. *J. Anal. Sci. Technol.* **15**, 19 (2024).
31. Bajo, K. -i et al. Depth profiling analysis of solar wind helium collected in diamond-like carbon film from Genesis. *Geochem. J.* **49**, 559–566 (2015).
32. Amari, S., Lewis, R. S. & Anders, E. Interstellar grains in meteorites: I. Isolation of SiC, graphite and diamond; size distributions of SiC and graphite. *Geochim. Cosmochim. Acta* **58**, 459–470 (1994).
33. Ziegler J. F., Biersack J. P., Ziegler M. D. *SRIM, the stopping and range of ions in matter*. Lulu Press Co., <http://www.srim.org> (2012).
34. Gallino, R., Busso, M., Picchio, G. & Raiteri, C. M. On the astrophysical interpretation of isotope anomalies in meteoritic SiC grains. *Nature* **348**, 298–302 (1990).
35. Kudritzki, R. P., Urbaneja, M. A. & Puls, J. Atmospheres and Winds of PN Central Stars. *Proc. Int. Astron. Union* **2**, 119–126 (2006).
36. Hultzsch, P. J. N. et al. Central stars of planetary nebulae in the Galactic bulge. *AA* **467**, 1253–1264 (2007).
37. Lodders, K. Relative atomic solar system abundances, mass fractions, and atomic masses of the elements and their isotopes, composition of the solar photosphere, and compositions of the major chondritic meteorite groups. *Space Sci. Rev.* **217**, 44 (2021).
38. Frew, D. J. & Parker, Q. A. Planetary Nebulae: Observational Properties, Mimics and Diagnostics. *Publ. Astron. Soc. Aust.* **27**, 129–148 (2010).
39. Kwok S. *The Origin and Evolution of Planetary Nebulae*. Cambridge University Press (2000).
40. O’Dell, C. R., McCullough, P. R. & Meixner, M. Unraveling the Helix Nebula: Its Structure and Knots. *Astronom. J.* **128**, 2339 (2004).
41. Milam, S. N., Woolf, N. J. & Ziurys, L. M. Circumstellar $^{12}\text{C}/^{13}\text{C}$ isotope ratios from millimeter observations of CN and CO: mixing in carbon- and oxygen-rich stars. *Astrophys. J.* **690**, 837–849 (2009).
42. Ramstedt, S., Schöier, F. L. & Olofsson, H. Circumstellar molecular line emission from S-type AGB stars: mass-loss rates and SiO abundances*. *Astron. Astrophys.* **499**, 515–527 (2009).
43. Obase, T., Bajo, K. -i, Otsuki, Y. & Yurimoto, H. Extreme solar particle ejection event in the last few million years from asteroid Itokawa sample. *Astrophys. J.* **978**, 142 (2025).
44. Yurimoto, H. et al. Quantitative analysis of helium by post-ionization method using femtosecond laser technique. *Surf. Interface Anal.* **48**, 1181–1184 (2016).
45. Tonotani, A. et al. Evaluation of multi-turn time-of-flight mass spectrum of laser ionization mass nanoscope. *Surf. Interface Anal.* **48**, 1122–1126 (2016).
46. Bajo, K. -i et al. Electronic data acquisition and operational control system for time-of-flight sputtered neutral mass spectrometer. *Surf. Interface Anal.* **51**, 35–39 (2019).
47. Bajo, K. -i et al. In situ helium isotope microimaging of meteorites. *Anal. Chem.* **96**, 5143–5149 (2024).
48. González-Santamaría, I., Manteiga, M., Machado, A., Ulla, A. & Dafonte, C. Gaia DR2 Distances to Planetary Nebulae. *Galaxies* **8**, 29 (2020).
49. Höfner, S. & Olofsson, H. Mass loss of stars on the asymptotic giant branch. *Astron. Astrophys. Rev.* **26**, 1 (2018).
50. Tosi, S. & Marini, E. Tracing the evolution of the emission properties of carbon-rich AGB, Post-AGB, and PN sources. *Astronomy* **4**, 2 (2025).
51. Höfner, S. & Freytag, B. Explaining the winds of AGB stars: Recent progress. *Proc. Int. Astron. Union* **16**, 165–172 (2020).
52. González et al. “Thermal” SiO radio line emission towards M-type AGB stars: A probe of circumstellar dust formation and dynamics. *Astron. Astrophys.* **411**, 123–147 (2003).
53. Schöier, F. L., Olofsson, H. & Lundgren, A. A. SiO in C-rich circumstellar envelopes of AGB stars: effects of non-LTE chemistry and grain adsorption. *Astron. Astrophys.* **454**, 247–255 (2006).
54. Ventura, P., Karakas, A., Dell’Aglia, F., García-Hernández, D. A. & Guzman-Ramirez, L. Gas and dust from solar metallicity AGB stars. *Mon. Not. R. Astron. Soc.* **475**, 2282–2305 (2018).
55. Kwok, S. From red giants to planetary nebulae. *Astrophys. J.* **258**, 280–288 (1982).
56. Kwok, S. Planetary Nebulae research: past, present, and future. *Galaxies* **12**, 39 (2024).

Acknowledgements

We thank Noriyuki Kawasaki for his assistance with the SEM observation. We thank Ryuichi Shimizu for his support during the development of LIMAS from the very beginning. This work was supported by JSPS KAKENHI (H.Y. and K.B.) and JST grants (H.Y.).

Author contributions

H.Y. conceptualized the initial idea. K.B., S.A. and H.Y. designed the study. S.A. carried out the sample preparation. K.B., T.I. and Y.O. carried out the LIMAS analysis and SEM observation. K.B., S.A. and H.Y. interpreted the data and wrote the paper, and all authors commented on it.

Competing interests

The authors declare no competing interests.

Additional information

Supplementary information The online version contains supplementary material available at <https://doi.org/10.1038/s41467-025-64216-1>.

Correspondence and requests for materials should be addressed to Hisayoshi Yurimoto.

Peer review information *Nature Communications* thanks Philipp Heck, Alexander Verchovsky, and the other anonymous reviewers for their contribution to the peer review of this work. A peer review file is available.

Reprints and permissions information is available at <http://www.nature.com/reprints>

Publisher's note Springer Nature remains neutral with regard to jurisdictional claims in published maps and institutional affiliations.

Open Access This article is licensed under a Creative Commons Attribution-NonCommercial-NoDerivatives 4.0 International License, which permits any non-commercial use, sharing, distribution and reproduction in any medium or format, as long as you give appropriate credit to the original author(s) and the source, provide a link to the Creative Commons licence, and indicate if you modified the licensed material. You do not have permission under this licence to share adapted material derived from this article or parts of it. The images or other third party material in this article are included in the article's Creative Commons licence, unless indicated otherwise in a credit line to the material. If material is not included in the article's Creative Commons licence and your intended use is not permitted by statutory regulation or exceeds the permitted use, you will need to obtain permission directly from the copyright holder. To view a copy of this licence, visit <http://creativecommons.org/licenses/by-nc-nd/4.0/>.

© The Author(s) 2025